Examine *Operando* Generated Ni-based Alloy Nanomaterials as Fuel Electrode in Solid Oxide Cells (SOCs)

X. Yue [z], A. Pukhova, S. He, N. Zhang

School of Chemistry, University of St Andrews, St Andrews, Fife KY16 9ST, UK

[z] xy57@st-andrews.ac.uk

Constructing nanostructure through exsolution has been demonstrated as an effective approach to produce electrode materials with superior performance and stability in the application of solid oxide cells, primarily due to the excellent catalytic properties as well as the significantly enhanced stability offered by the well-embedded nanoparticles that are exsolved from a supporting oxide. In this work, we focus on investigating the titanate perovskites with exsolved Ni-Co alloy nanocatalysts as fuel electrode of solid oxide cells (SOCs), particularly on *operando* generating these nanomaterials via applying a potential bias in CO_2 electrolysis operating conditions. Three compositions of titanate perovskite were examined, including $La_{0.43}Ca_{0.37}Ti_{0.94}Ni_{0.06}O_{3-\delta}$ (LCT-Ni6), $La_{0.43}Ca_{0.37}Ti_{0.94}Ni_{0.03}Co_{0.03}O_{3-\delta}$ (LCT-Ni3Co3), and $La_{0.43}Ca_{0.37}Ti_{0.90}Ni_{0.05}Co_{0.05}O_{3-\delta}$ (LCT-Ni5Co5). Various techniques, including X-ray diffraction, thermogravimetric analysis, DC conductivity measurement etc., were applied to study the crystal structure, reduction behavior, conductivity property and microstructure of these materials. SOCs with these titanate fuel electrodes were fabricated and evaluated, with emphasis placed on *operando* generation of active nanomaterials through electrochemical switching in pure CO_2 atmosphere, and on understanding the materials properties linking to their microstructure and performance towards CO_2 electrolysis and H_2 fuel cell.

Introduction

Solid oxide cells have been considered as one of the core technologies in the future energy systems that rely heavily on renewable energy resources, such as solar, wind etc., due to the unrivaled high conversion efficiency they offer (1). SOC can work in solid oxide fuel cells (SOFCs) mode converting chemical energy in H_2, CH_4 and other hydrocarbon and biomass, to electricity and heat with mitigated environment impact. The same device can reversely operate in solid oxide electrolysis cells (SOECs) mode, using electricity to split steam, CO_2 and the mixture to produce H_2, CO and syngas, which can be directly used as fuel or further processed to chemicals and synthetic fuels, displacing fossil fuels. When renewable electricity is used to drive the splitting reactions, SOCs offer an excellent pathway to store the intermittent and decentralized renewable resources into forms that are more convenient and resilient for utilization. Significant development and improvement have been made in SOCs technology in the last decade, however, further advances at the level of cell, stack and systems are still needed to improve performance, durability and lower cost for eventual commercialization of this technology.

Constructing nanostructured electrodes have been demonstrated as an effective approach to enhance performance and durability of SOCs, primarily due to markedly extended triple phase boundaries (TPBs), where the active electrochemical reaction zone locates (2). Infiltration has been widely adopted for fabricating nanostructured electrodes, however, there are problems associated with this approach that are difficult to tackle, such as catalyst coarsening and the resultant performance degradation in long term operation (3, 4). Exsolution, as an alternative, has become increasingly attractive in recent years, due to its capability of generating uniformly distributed fine particles that are strongly embedded into the surface of their parent oxide, offering excellent particle stability against coarsening and coking (5-7). By tailoring the non-stoichiometry and dopant size, a wide range of metal and metal alloy nanoparticles have been fabricated by this manner, such as Ni (5, 6), Co (8), NiFe (9-11), NiCo (7), CoFe (12) and so on, among which alloy nanocatalysts are particularly interesting owing to their enhanced catalytic properties and promoted stability compared to single metal counterpart.

In exsolution processing, nanoparticles can be produced either *in-situ* by exposing to a H_2-containing atmosphere or *operando* by applying a potential bias in an SOEC, referred to as electrochemical switching. It was reported that, although the potential-reduction seemed to follow the same raw as the chemical reduction, exsolution of pinned nanoparticles occurred almost instantly at 2.0 V in steam electrolysis operating condition, with sufficiently high amount and smaller particle sizes (13). In contrast, exsolution by chemical reduction takes hours even days, yet with less impressive performance. This indicates that electrochemical reduction by applying suitable potential or current can serve as an efficient method to produce electrocatalysts in nanoscale, which is well suited to SOEC operations, where fuel electrode materials decorated with nanocatalysts can be produced *operando*, bringing simplicity and cost-effectiveness in fabrication. However, so far chemical reduction was predominantly applied in literature as a pathway to introduce nano-scaled catalyst, leaving the potential-driven exsolution not being extensively studied, especially in CO_2 electrolysis via SOECs.

To that end, efforts have been made to investigate *operando* generation of nanomaterials in CO_2 atmosphere and their applications as fuel electrodes in SOCs, particularly Ni-based alloy nanomaterials. In the present work, two compositions of Ni and Co co-doped titanate perovskite were synthesized and characterized, and as a comparison, solely Ni doped titanate analogue was also prepared and tested. The focus was placed on producing active nanomaterials through electrochemical switching in CO_2 atmosphere, and on understanding the materials properties linking to their microstructure and performance.

Experimental

Material Synthesis and Characterizations

The materials of interest, $La_{0.43}Ca_{0.37}Ni_{0.06}Ti_{0.94}O_{3-\delta}$ (LCT-Ni6), $La_{0.43}Ca_{0.37}Ni_{0.03}Co_{0.03}Ti0_{.94}O_{3-\delta}$ (LCT-Ni3Co3) and $La_{0.43}Ca_{0.37}Ni_{0.05}Co_{0.05}Ti0_{.90}O_{3-\delta}$ (LCT-Ni5Co5), were synthesized following a modified solid-state synthesis route that was reported previously (5). Briefly, La_2O_3 (Pi-Kem, 99.99%), $CaCO_3$ (Alfa Aesar, 99.99%), TiO_2 (Alfa Aesar, 99.6%), $Ni(NO_3)_2 \cdot 6H_2O$ (Acros, 99%) and $Co(NO_3)_2 \cdot 6H_2O$ (Acros, 99%), with stoichiometric ratios according to composition, were weighed and mixed. The oxide and carbonate precursors were dried overnight prior to weighing, with La_2O_3 at 850°C and $CaCO_3$, TiO_2 at 300°C, and they were weighed while still warm. This was helpful to get accurate weights so to assist successful synthesis. All the precursors, with a small amount (~1 wt.%) of Hypermer KD-1 dispersant, were then mixed homogeneously in acetone using high energy ultrasonic probing (Hielscher UP200S). The resulting precursor slurry was subsequently placed on a hot plate to evaporate the acetone, leaving behind a powder mixture, which was calcined at 1000°C for 12h. The calcined powder was then ball-milled for 2h in a planetary ball miller to ensure homogeneity, before being pressed into dense pellets and sintered at 1400°C for 10h.

The dense pellets were then crushed and ground to fine powders. X-ray diffraction (XRD) was measured using a PANalytical Empyrean X-ray diffractometer with Cu-$K_{\alpha 1}$ radiation in reflection mode to identify the crystal structure and phase purity of the as-synthesized materials. The samples were scanned in the two-theta range of 20-90 degree with a step size of 1.2°/min. The phases presented in the XRD patterns were indexed with the Xpert HighScore plus software to determine the crystal structure. Rietveld refinement was also performed based on the measured XRD patterns, using GSAS-II software.

Thermogravimetric analysis (TGA) was carried out to monitor the weight change of the as-synthesized titanate materials during reduction. A Netzsch STA 449C instrument was used for TGA measurement, in which the samples were heated up to 900 °C in 5% H_2/N_2, followed by a 10-hour isothermal reduction before cooling down to room temperature. The ramp rate was kept constant at 5 °C/min. The mass loss from the Ni and Ni-Co co-doped titanates in the reducing atmosphere was analyzed and compared, to investigate the impact of Ni-Co co-doping over solely Ni doping on the reduction behavior of the perovskite.

The DC conductivity characterization was conducted to study exsolution of metallic nanoparticles on the conductance of the titanates, as well as to look into how Ni and Co co-doping affects the material's conduction properties as compared to that with only Ni doping. A particle size control was carried out for which the as-synthesized powders were ball-milled to reach a $d_{50} = 1.4\pm0.2$ μm for all samples. The samples were then mixed with varying amount of graphite (Alfar Aesar) and rice starch (Sigma Aldrich) until homogenous, with the latter two served as pore formers to introduce extra porosity to facilitate gas diffusion hence reduction of the perovskite. The powder mixture was then pressed into a bar under 1 ton of pressure and fired at 1200-1250 °C. Au wires were attached to the bar sample, prior to the four-point DC conductivity measurement. The samples, placed in a tubular furnace, were heated to 900 °C (at 5 °C/min) in 5% H_2/N_2 gas and held at 900 °C for 20 hrs to allow sufficient reduction take place. Following isothermal reduction, the samples were cooled down to room temperature in the same atmosphere. The conductance of the samples was recorded in the whole course of heating, dwelling and cooling in reducing atmosphere.

TABLE I. Summary of the bar samples preparation conditions and their porosity after sintering

Sample	Sintering temperature (°C)	Graphite (wt. %)	Rice starch (wt. %)	Porosity* (%)
LCT-Ni6	1250	20	20	32
LCT-Ni3Co3	1250	20	20	18
LCT-Ni3Co3	1200	40	20	50
LCT-Ni5Co5	1200	40	20	54

* The porosity was obtained by comparing the relative density (using the mass and dimensions) of the sintered sample to the theoretical density calculated from the Rietveld refinement of XRD results (shown in **Table II**).

Through our experiment, it was found that Co doping significantly altered the sintering behavior of the titanate compared to the Ni doped counterpart. When using identical amount of pore formers and sintering temperature, the samples with Co doping shrank greatly, yielding much lower porosity than that without Co. Therefore, different amount of pore formers and sintering temperature were adopted in preparing the Ni and Co co-doped bar samples, as summarized in Table I. After sintering, the porosity of the obtained-bar sample was evaluated using the weight over dimensions method and comparing to the theoretical density obtained from XRD refinement. To term the samples with different porosity, the porosity value was added as suffixes to the compositions, for instance, LCT-Ni6 with porosity of 32% was termed as LCT-Ni6-p32%.

Solid Oxide Cell Fabrication and Electrochemical testing

Electrolyte supported structure was adopted in single cell fabrication. The 10 mol.% Scandium and 1 mol.% cerium stabilized zirconia (denoted as ScSZ herein, DKKK) electrolyte was prepared from aqueous tape casting, followed by lamination and sintering at 1400°C. The thickness of the as-prepared electrolyte support was ca. 120 μm.

Electrodes were screen printed on the electrolyte support and fired at different temperatures. Concerning fuel electrode, the as-synthesized LCT-Ni6, LCT-Ni3Co3, and LCT-Ni5Co5 powders was subjected to the same particle size control as that in conductivity sample preparation, after which each powder sample was mixed with KD-1 dispersant, terpineol, and polyvinyl butyral (PVB), respectively, to form homogeneous ink that was suitable for screen printing. As to air electrode, the standard lanthanum strontium mangante $(La_{0.8}Sr_{0.2})_{0.95}MnO_3$ (LSM, Pi-KEM) was mixed with ScSZ electrolyte with a weight ratio of 50-50, and prepared into LSM-ScSZ screen-printing ink in a similar fashion as the fuel electrode ink. Pure LSM ink was also made and printed on top of the LSM-ScSZ for better current collection. After screen printing, the fuel electrodes were fired at 1250-1150 °C, and the air electrode was fired at 1100 °C. The thickness of the fuel electrode and air electrode was ca. 20 μm and 30 μm respectively.

Prior to electrochemical testing, Au wires were attached to both the fuel electrode and the air electrode as current collector. The cell was mounted to an alumina tube that was serving as fuel chamber and sealed with cerambond (Aremco #552). The whole kit was placed vertically in a temperature-programed furnace and heated to 900 °C in air. Upon reaching 900 °C, pure CO_2 at a flow rate of 50 ml/min was supplied to the fuel chamber. Subsequently, a potential bias of 2V was applied to the cell for a duration of 5min, also known as electrochemical switching (13), in order to generate electrocatalytically active nanocatalysts. The electrochemical switching was repeated 4-5 times to obtain sufficient exsolution for enhanced electrode performance. Polarization curve (i.e. I-V curve) as well as electrochemical impedance spectroscopy (EIS) in CO_2 electrolysis operating conditions were recorded before and after the electrochemical switching. A multichannel Solartron 1470B coupled with a 1252A frequency response analyzer were used for electrochemical characterization, and EIS was collected with an amplitude of 20 mV and frequency ranging from 100 kHz to 0.1 Hz. The cell performance in fuel cell mode was also characterized after testing in CO_2. A humidified (3% H_2O) H_2 at a flow rate of 40 ml/min was flushed to the fuel chamber and I-V curve as well impedance spectra were measured.

Post-mortem Microstructure Analysis

Scanning electron microscopy (SEM) was employed to examine the microstructure and morphology of the samples after conductivity measurement and electrochemical test respectively. A FEI Scios dual beam microscope was used for that purpose, and Energy dispersive X-ray spectroscopy (EDS) was coupled with SEM for compositional analysis.

Results and discussion

Crystal Structure Analysis of the Ni Doped and Ni-Co Co-doped Perovskite

Figure 1(a) shows the XRD patterns of the as-synthesized LCT-Ni6, LCT-Ni3Co3, and LCT-Ni5Co5 material. It is clear that all samples had formed pure perovskite structure after the solid-state synthesis. Upon partially replacing Ni with Co, the diffraction peaks of the perovskite shift towards lower two-theta angles, as reflected in Figure 1 (b) where a closer look at the framed region in Figure 1(a) is shown. The perovskite diffraction peaks move further towards low angles when the Ni and Co co-doping level is increased, as revealed in the LCT-Ni5Co5 sample. The left-shift of the diffraction peaks in Figure 1 indicates that the d spacing and therefore, the unit cell parameters of the perovskite becomes larger upon Co doping, according to Bragg's law. This agrees well with the fact that ionic radius of the Co (II) with six coordination is larger than that of Ni (II) (six coordinated), which is Co *vs.* Ni 0.745 Å *vs.* 0.69 Å, both are larger than the Ti (IV) ionic radius, 0.605 Å.

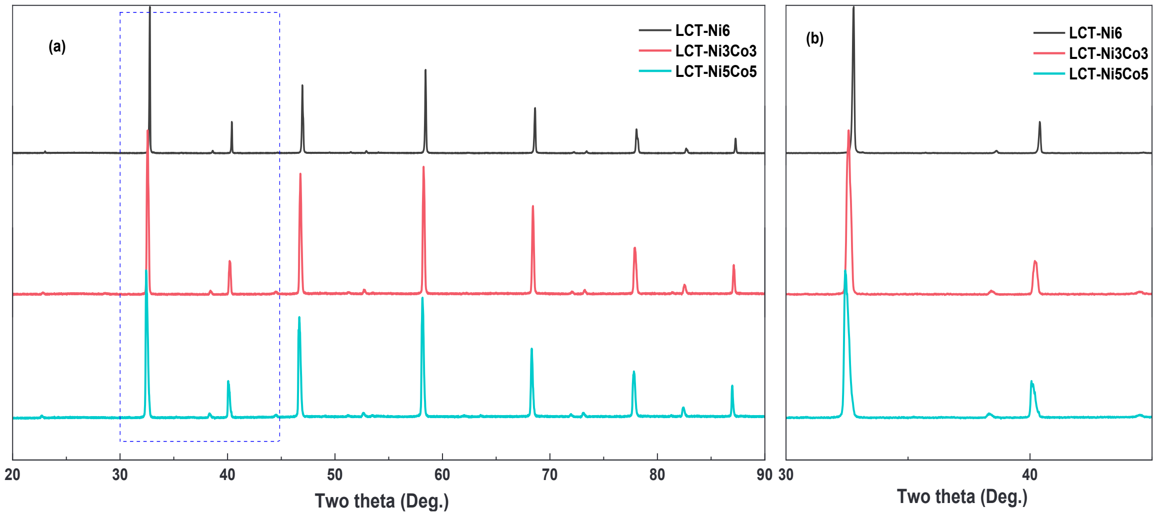

Figure 1. (a) Room temperature XRD pattern of the as-synthesized powders and (b) a closer look at the two-theta range of 30-45° (i.e. the framed region in (a)).

TABLE II. Summary of the Rietveld refinement results

	LCT-Ni6	**LCT-Ni3Co3**	**LCT-Ni5Co5**
Space group	Ibmm	Ibmm	Ibmm
Cell parameters (Å)	a=5.47494 b=5.47135 c=7.72731	a=5.47535 b=5.47504 c=7.72888	a=5.47949 b=5.47964 c=7.73545
V (Å^3)	231.474	231.695	232.262
Density (g/cm^3)	4.9097	4.9050	4.9065
Rietveld refinement parameters	wR_P=10.09%, GOF = 1.8	wR_P=9.29%, GOF = 1.61	wR_P=12.14%, GOF = 2.04

Table II summaries the results from Rietveld refinement of the measured XRD patterns. An orthorhombic structure is assigned to all the three compositions synthesized in this work.

With partial substitution of Ni with Co, the unit cell parameters increase with increasing Co doping level, so does the unit cell volume. This trend agrees with what was indicated based on the peak shift phenomena observed in Figure 1.

TGA of the Ni Doped and Ni-Co Co-doped Perovskite

The TGA profile of the as-synthesized LCT-Ni6, LCT-Ni3Co3 and LCT-Ni5Co5 is displayed in Figure 2, which reveals the mass change in the perovskites during reduction in 5% H_2/N_2 up to 900 °C. Upon reduction, the titanate perovskite loses its lattice oxygen, therefore, weight loss is expected on the TGA profile. In Figure 2, except some initial weight changes at lower than 150°C, there were no significant weight loss at lower than 600 °C. At higher than 650°C, the weight loss becomes massive on all three samples being examined, and greater mass loss can also be observed during the isothermal reduction at 900 °C attributed to faster kinetics at elevated temperatures. However, one can also see in Figure 2(b) that with elongation of reduction time at 900 °C, the weight loss gradually becomes mild due to the slow reduction of Ti^{4+} in the bulk. It can be obtained from Figure 2 (a-b) that the difference in mass from onset until the end of isothermal reduction is 0.40% in LCT-Ni6, and when replacing half of Ni with Co in LCT-Ni6, the difference reaches 0.45%, slightly higher than solely Ni doped titanate. Nevertheless, the weight loss from onset until the end of dwelling at 900 °C achieves 0.61% in LCT-Ni5Co5, which is much higher than that in LCT-Ni6. These indicate that the introduction of some Co on the B-site is beneficial for promoting the reductivity of the titanate perovskite, which might contribute to enhanced conductivity as discussed in the following part.

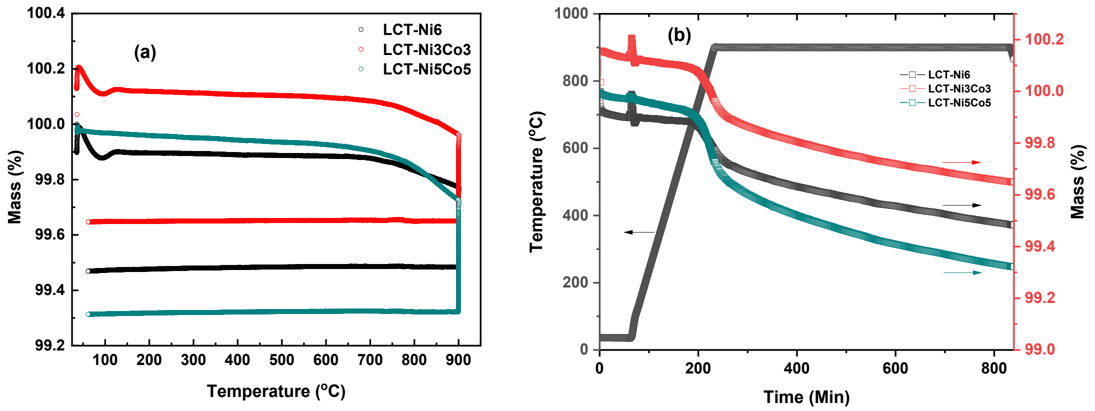

Figure 2. TGA profile of the titanate powder samples with different B-site doping upon reduction in 5% H_2/N_2 with (a) weight vs. temperature and (b) weight and temperature vs. time.

Conductivity and Post-mortem Analysis of the Ni Doped and Ni-Co Co-doped Perovskites

The conductivity of the Ni as well as Ni-Co doped titanate was measured to study the impact of Co doping on the titanate's conduction property. The measurement was done in 5% H_2/N_2, in which exsolution of metallic or bimetallic nanoparticles took place during reduction affecting conductivity. The conductivity the LCT-Ni6-p32% sample is shown in Figure 3(a), in which its conduction behavior upon reduction is illustrated during heating up, dwelling at 900 °C (20 hrs) as well as cooling in 5% H_2/N_2 atmosphere. At lower than 650°C during heating up, the conductivity of the LCT-Ni6 stays low and changes little with temperature, however, it increases sharply with temperature at higher than 650 °C. This coincides with the onset of reduction at higher than 650°C from the TGA results in Figure 2. As a n-type conductor, the titanate perovskite shows increasing conductivity with decreasing P_{O2}, therefore, the higher the extent of reduction, the higher the conductivity it possesses. The sharp increases in conductivity at higher than 650ºC is also associated with the exsolution of metal nanoparticles which facilitate the reduction of titanate perovskite. Upon reaching 900 ºC and holding for 20 hrs, the conductivity of LCT-Ni6 continues to increase greatly until the end of the dwelling stage, and afterwards it decreases with lowering temperature. Similar conduction behavior was also seen on the titanates with both Ni and Co dopants, regardless of their porosity.

The comparison of conduction behavior between the Ni doped and the Ni-Co co-doped titanates with different porosity is reflected in Figure 3(b), in which data from cooling stag in conductivity measurement was plotted against temperature. One can observe that, regardless of porosity in different samples, the incorporation of Co enhances the conductivity of the titanate, especially at higher temperatures. This is probably due to the introduction of multivalence on the B-site as Co is known to have multiple valences. In Figure 3(b), except the LCT-Ni3Co3-p18% that has the lowest porosity (highest density), the Ni doped titanate and the Ni-Co co-doped titanates that have higher porosities present little changes in their conductivity values initially with lowering temperature, and as temperature drops to lower than, e.g. 550ºC, they all show significantly decreased conductivity, which is typical for a semiconductor. In the case of the LCT-Ni3Co3-p18%, the conductivity firstly increases with decreasing temperature, following a metal-type conduction behavior, and at temperatures lower than 550ºC the conductivity decreases with lowering temperature, transforming to a semiconductor behavior.

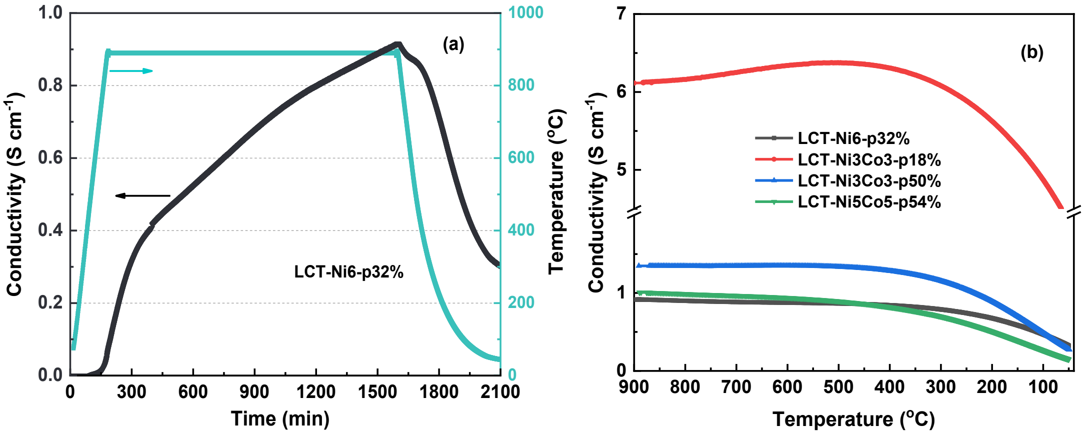

Figure 3. Conductivity measurement for (a) LCT-Ni6 during heating up, holding at 900 ºC and cooling down and (b) samples with different B-site dopant and varying porosity during cooling down. The atmosphere was kept identical for all samples, which was 5% H_2/N_2 at 40 ml/min

It is obvious from Figure 3(b) that the sample porosity impacts its conduction property and behavior significantly. As mentioned in the Experimental section, the introduction of Co into the perovskite lattice increased the sintering of the material. When the same amount of pore formers and identical sintering temperature were adopted (Table I), the 3 mol% Ni and 3 mol.% Co co-doped titanate bar sample (LCT-Ni3Co3) has appreciably lower porosity than the 6 mol.% Ni doped titanate (LCT-Ni6) bar sample after sintering, which is 18% *vs.* 32%, with the former possessing dramatically higher conductivity than the latter in Fig. 3(b). When using higher amount of pore formers and in the meantime lower sintering temperature, the porosity of the Ni and Co co-doped titanate (LCT-Ni3Co3-p50% and LCT-Ni5Co5-p54%) increase considerably but their conductivity have dropped markedly. In Figure 3(b), the conductivity of the LCT-Ni3Co3-p18% sample is almost six times higher than that of the more porous LCT-

Ni3Co3-p50% sample. The possible reason for the lower conductivity in the highly porous Ni and Co doped samples is that with lowered sintering temperature, the grain size decreases significantly with more grain boundaries built up (see SEM images in the following part) which probably impede the electron and ion diffusions leading to lower conductivity. Despite higher porosity (greater than 50%), the Ni and Co co-doped sample still exhibits higher conductivity than the solely Ni doped sample (LCT-Ni6) does after reduction, suggesting Ni and Co co-doping is beneficial for improving the material's conductivity compared to solely Ni doping. This agrees with what was revealed from the TGA results in Figure 2.

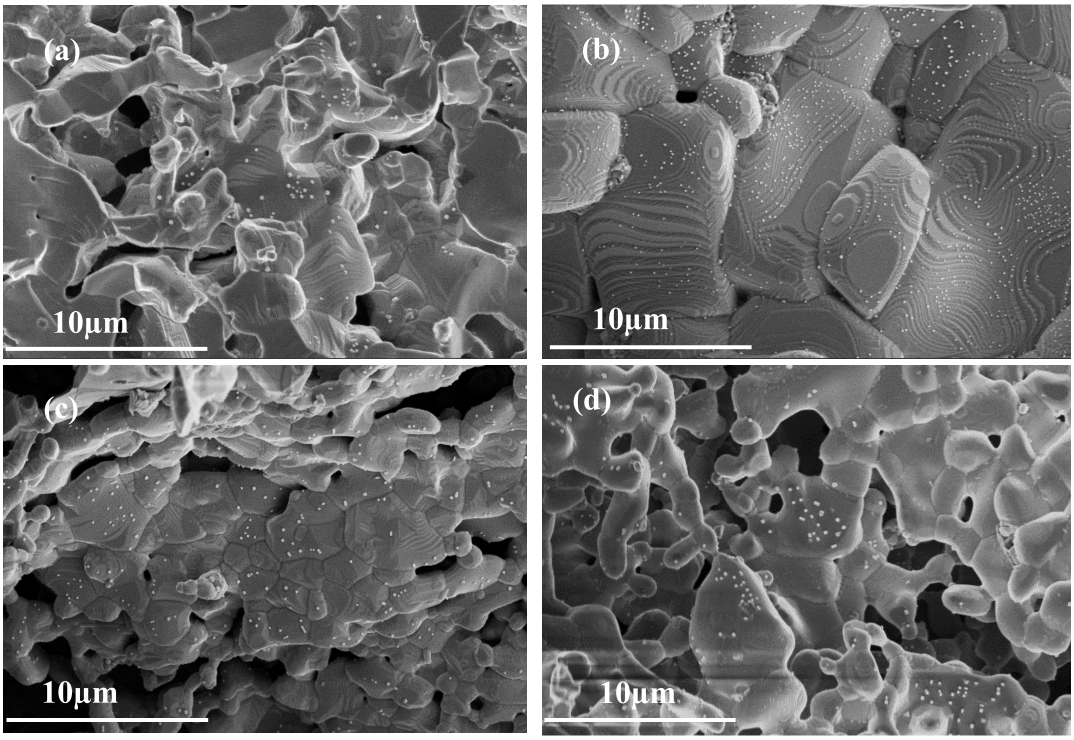

Figure 4. SEM micrographs of the samples after the conductivity measurement. (a) LCT-Ni6-p32%; (b) LCT-Ni3Co3-p18%; (c) LCT-Ni3Co3-p50%, and (d) LCT-Ni5Co5-p54%

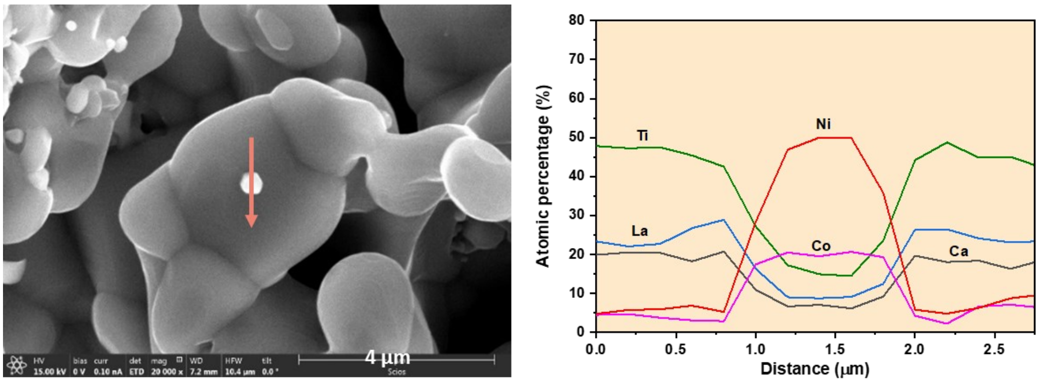

Figure 5. SEM-EDS analysis obtained from the LCT-Ni5Co5-p54% sample. A EDS line scan was conducted along the red line on the SEM image (on the left-hand side) with the compositional analysis result shown on the right-hand side

The microstructure of the samples after conductivity characterization was inspected by SEM, as displayed in Figure 4. Generally, nanoparticles with diverse populations and sizes are observable on different samples in Figure 4. Comparing to the perovskite with Ni mono-metal dopant (Figure 4(a)), the 6% and 10% Ni-Co co-doped perovskite have more nanoparticles formed on the surface after reduction, of which the one has the lowest porosity (Figure 4(b)) presents nanoparticles with distinctively smaller size and higher population. Indeed, the Ni-Co co-doped titanate perovskites has shown higher weight loss (Figure 2) and higher conductivity after reduction (Figure 3(b)) than the solely Ni doped counterpart. As to the composition of the nanoparticles produced on the Ni and Co co-doped sample, e.g., LCT-Ni5Co5-p54%, the SEM-EDS analysis in Figure 5 confirms their bimetallic nature. Indeed, only Ni and Co are detected in the line scan across the nanoparticle in Figure 5, with a Ni/Co ratio around 3/1.

With Ni and Co co-doping, after firing at higher temperature (1250°C), the sample has sintered significantly compared to those fired at lower temperature (1200°C) and to the sole Ni doped samples at the same temperature (1250°C). In Figure 4(b), one can see that the grains from the Ni and Co co-doped sample sintered at higher temperature (thus lowest porosity) are much larger than those from the samples sintered at lower temperature. The remarkably smaller yet higher population nanoparticles on this sample indicates the occurrence of higher extent of reduction in this material, yielding profoundly higher conductivity. On contrast, the Ni and Co co-doped samples sintered at lower temperature exhibit much smaller grains and appreciably more grain boundaries, which probably results in higher resistance for electron and ion diffusions during reduction leading to lower level of reduction in the materials and consequently lower conductivity (Figure 3(b)) and less nanoparticles (Figure 4(c-d)).

Operando generation of electrocatalysts as well as their performance in SOCs

In this part, efforts were made to *operando* generate nanocatalysts under the CO_2 electrolysis working conditions and to evaluate the performance of the titanate electrode with Ni and Co co-doping compared to that with sole Ni doping. Single cells with the same electrolyte and air electrode but different fuel electrodes, with LCT-Ni6, LCT-Ni3Co3, and LCT-Ni5Co5, were tested respectively. For *operando* generation of nanocatalysts, an electrolysis voltage of 2V was applied to single cells at 900 °C in pure CO_2, without any pre-reduction being carried out. The switching was repeated 4-5 times with 5min duration each time to drive sufficient exsolution.

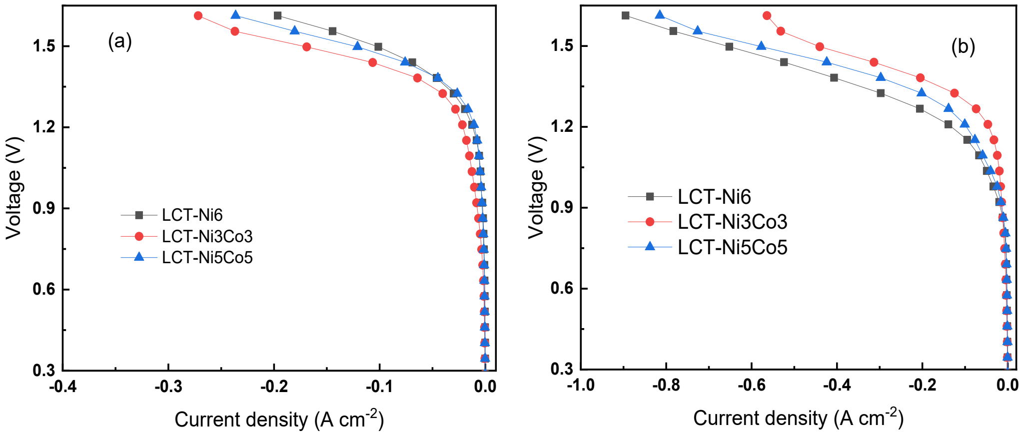

Figure 6. Comparisons of I-V curves of the cells with LCT-Ni6, LCT-Ni3Co3, and LCT-Ni5Co5 fuel electrode working in pure CO_2 atmosphere at 900 °C. (a) before and (b) after electrochemical switching

Figure 6 displays the I-V curves of the cells with different fuel electrode working in electrolysis mode at 900 °C in CO_2 atmosphere, before and after electrochemical switching at 2V. As expected, the cells show poor performance before switching, achieving only 0.1-0.18

A cm^{-2} of current density at 1.5 V in Figure 6(a). After potential-driven reduction, the current density values are drastically enlarged in Figure 6(b), reaching 0.45-0.65 A cm^{-2} in the same conditions as before switching, owing to the activation of the fuel electrode material during switching. Indeed, nanoparticles are seen on the surface of the fuel electrode after switching (Figure 10), in contrast to the smooth and clean surface from a fresh electrode (as displayed in Figure S1). Comparing Figure 6 (a) and (b), one can see that the Ni and Co co-doped electrodes perform better than the merely Ni doped titanate electrode towards CO_2 electrolysis before switching. However, after switching both the LCT-Ni3Co3 and the LCT-Ni5Co5 electrodes perform unfavorable for CO_2 electrolysis compared to the Co free LCT-Ni6 electrode. The latter has the highest current density, 0.65 A cm^{-2} at 1.5 V after electrical reduction at 2V. Worth mentioning that the Co free LCT-Ni6 electrode was fired at 1250 °C whereas the Ni and Co co-doped electrodes were fired at 1150 °C. Firing the co-doped electrodes at higher temperature, e.g., 1250-1200 °C caused not only the densification of the electrode microstructure leading to limited gas diffusion, but also the delamination of the fuel electrode from electrolyte due to the mismatched shrinkage. A sintering temperature of 1150 °C was therefore adopted in this work as a trade-off for the Ni-Co doped electrodes, and the fired electrode were seemingly porous and no signs of delamination after sintering.

The impedance spectra of the cells with different fuel electrode were recorded at 1.35V under CO_2 electrolysis mode at 900°C, before and after electrochemical switching. Figure 7 shows an example of the EIS that is from the LCT-Ni6 fuel electrode cell. On impedance spectrum, the observed impedance arcs denote the electrochemical processes taking place on the electrodes with their magnitude indicating the easiness of these processes. The intersects of the impedance arcs with the real axis at high frequency and low frequency range stand for series impedance, or ohmic resistance (Rs) in other words, and total resistance respectively, with the difference between the two representing polarization resistance (Rp). In Figure 7, a feature of substantially decreased impedance arcs, especially the one locates at low frequency region (0.15-5 Hz), is seen after electrochemical switching, suggesting facilitated electrode processes as a result of enhanced electrocatalytic activity from the fuel electrode after switching. This is consistent with the enlarged current density from the I-V curve after switching (Figure 6b). Repeating switching leads to further reduced impedance arcs, hence continuously improved catalytic properties towards CO_2 electrochemical reduction. The phenomenon is most profound from the first three switching but becomes marginal after the fourth switching.

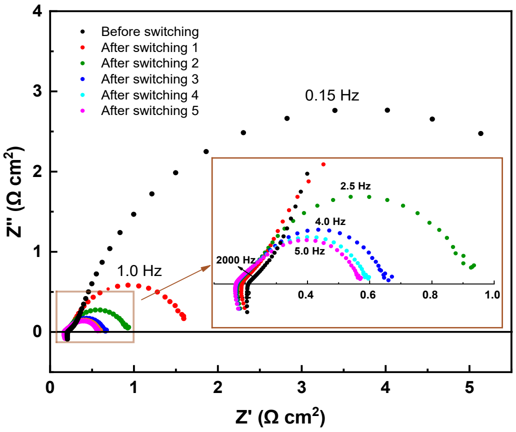

Figure 7. Impedance spectra of the LCT-Ni6 cell operating at 1.35 V in CO_2 at 900 °C before and after electrochemical switching. The inset shows a zooming in at the framed area on the impedance spectra.

Similar trends were obtained from the cells with the Ni and Co co-doped titanate electrodes. To aid clear comparison, the Rs and Rp values from the EIS of the cells with various fuel electrode operating in identical conditions were extracted and plotted against number of switching in Figure 8. A general observation is that, after the activation of the fuel electrodes via electrochemical switching, both Rs and Rp values have diminished. With increasing numbers of switching, i.e., extending the switching time, the changes in Rs and Rp become smaller, for instance, the variations in the Rs and Rp values are trivial after the third switching, implying that further extending the switching time (longer than 15 min) at 2V is probably helpless to further boost the electrode activity.

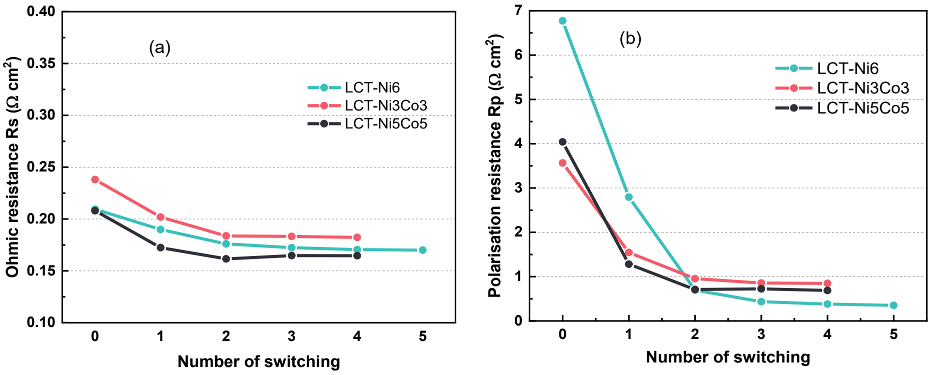

Figure 8. (a) Ohmic resistance Rs and (b) polarization resistance Rp of the cells with different fuel electrode *vs.* numbers of electrochemical switching. Rs and Rp values were obtained from the impedance spectra of the respective cell working at 1.35V at 900°C in pure CO_2 50ml/min, after electrochemical switching at 2V for 5min each time

In Figure 8(a), the Rs values fall in the range of 0.16-0.18 Ω cm^2 after potential-driven reduction whereas they are greater than 0.2 Ω cm^2 before electrochemical switching, which is not surprising as the conductivity of the titanate perovskite increases upon reduction (Figure 3(a)). The insignificant reduction in Rs, comparing to that of Rp, is originated from the minor lateral contribution from electrodes compared to the predominant cross contribution from electrolyte. As to the Rp, the values after switching drop tremendously, reaching one magnitude lower than those before switching. The Rp values from the cell with the LCT-Ni6 fuel electrode are 6.8 Ω cm^2 *vs.* 0.4 Ω cm^2 before and after switching, with the Rp values from the LCT-Ni5Co5 electrode reaching 4.0 Ω cm^2 *vs.* 0.7 Ω cm^2 before and after switching in Figure 8(b). A dramatic decrease in Rp was also reported previously with increasing the switching potential, due to the exsolution of metallic nanocatalyst particles on the surface of the fuel electrode promoting its electrocatalytic properties (14). Interestingly in Figure 8(b), the cells with the Ni-Co co-doped titanate electrode present considerably lower Rp values than that with only Ni doped electrode before switching, which is still the case after the first switching, whereas after the second switching the Rp values from the former becomes larger than the latter. This matches with the observations from the I-V curves (Figure 6) before and after switching. If one recall, with Ni and Co co-doping the titanates demonstrate higher weight loss and higher conductivities than that with only Ni doping during reduction in 5% H_2/N_2, which might interpret the higher performance from the former when adopted as SOC fuel electrode. Nevertheless, the phenomenon that the former performs poorer than the latter in CO_2 electrolysis after the second switching implies careful engineering of either the microstructure of the Ni-Co co-doped titanates electrode or the electrochemical switching conditions is needed to optimize the *operando* generation of nanocatalysts in the case of Ni-Co co-doped electrode.

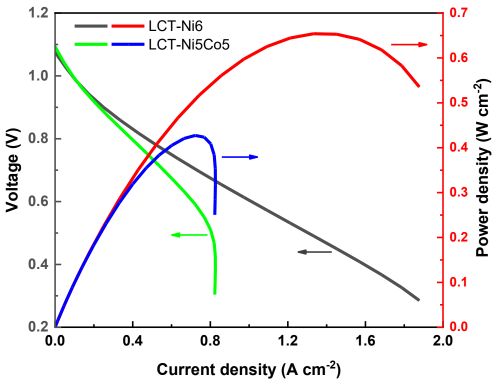

Figure 9. Performance of the SOCs with LCT based fuel electrodes working in wet H_2 (3% H_2O) at 900 °C after electrochemical switching in CO_2 electrolysis

After switching and performance evaluation in CO_2 atmosphere, humidified H_2 (3% H_2O) was switched on and the cell performance was characterized in fuel cell mode. Figure 9 displays the I-V curves and the corresponding power outputs from the cells with LCT-Ni6 and that with LCT-Ni5Co5 fuel electrode. The cell with the LCT-Ni3Co3 fuel electrode developed minor leaks after switching leading to a lower OCV value (see Figure S2), thus it's not included in Figure 9. The Co free LCT-Ni6 electrode cell displays a higher max. power density than the Ni-Co co-doped electrode cell, which is 0.65 *vs.* 0.43 W cm^{-2} at 900 °C in 3% H_2O/H_2. It is not surprising to see that the performance of fuel electrode with both Ni and Co dopants is inferior to that with only Ni doping in H_2 fuel cell operation, as the fuel electrodes were activated under CO_2 electrolysis working conditions and poorer performance was readily seen from the Ni-Co co-doped titanate electrodes after the second switching in Figure 8(b). In Figure S2 and Figure 9, a limiting current density is seen on the LCT-Ni3-Co3 and LCT-Ni5Co5 electrode cells while it is not presented on the LCT-Ni6 electrode cell, implying that the microstructure or the switching conditions of the electrode with Ni and Co dopants need to be optimized to mitigate mass diffusion restrictions.

The post-mortem microstructure analysis of the cells after electrochemical testing is shown in Figure 10. Both the fuel electrode and air electrode were well bonded to the electrolyte after testing (see Figure S3). In Figure 10, nanoparticles formed from electrochemical switching are seen on all the fuel electrodes under study. This explains the origin of the promoted cell performance towards CO_2 electrolysis after switching, as seen in Figure 6-8. A careful inspection reveals a uniform distribution of nanoparticles decorating on the surface of the LCT-Ni6 electrode across the whole thickness, as fine nanoparticles are readily seen on the outer area (Figure 10(a2)) as well as on the inner area (Figure 10(a1)) of the electrode. However, uneven distribution in the meantime less nanoparticles were found on the LCT-Ni3Co3 and LCT-Ni5Co5 electrodes. On the LCT-Ni3Co3 electrode, *operando* generated nanoparticles are mainly locating at the inner area (Figure 10(b1)), i.e., the area close to the electrode/electrolyte interface, whereas they are barely seen at the outer area of the electrode (Figure 10(b2)). Such non-uniform distribution of nanocatalysts is probably the cause of the limited performance improvement in Ni-Co co-doped titanate electrode after switching. On the LCT-Ni5Co5 electrode (Figure 10 (c1, c2)), again the nanoparticles produced under *OPERANDO* conditions are not homogeneously located, with a lower density than that on the LCT-Ni6 electrode. These interpret why the Ni-Co co-doped electrodes displayed lower activity compared to that of the Co free LCT-Ni6 electrode towards CO_2 electrolysis (Figure 6 and 8) and H_2 fuel cell (Figure 9) after electrochemical switching. The reason for the ineffective switching from the Ni-Co co-doped fuel electrodes may stem from their striking microstructure compared to the solely Ni doped counterpart, as exhibited in Figure 10 (a, b, c). As mentioned previously, applying the same sintering temperature that was used in LCT-Ni electrode led to markedly densified microstructure in the Ni-Co doped electrodes, whereas simply lowering the sintering temperature didn't bring optimized microstructure either. Given the promoted reductivity and conductivity as a result of Ni and Co co-doping as well as the superior electrocatalytic activity from co-doped electrodes before switching (and after the first switching), it is necessary to carry on some microstructure engineering as well as optimization of switching conditions to improve the efficiency of switching on these electrodes, to bring higher activity than the solely Ni doped analogue. This will be the focus of our future work.

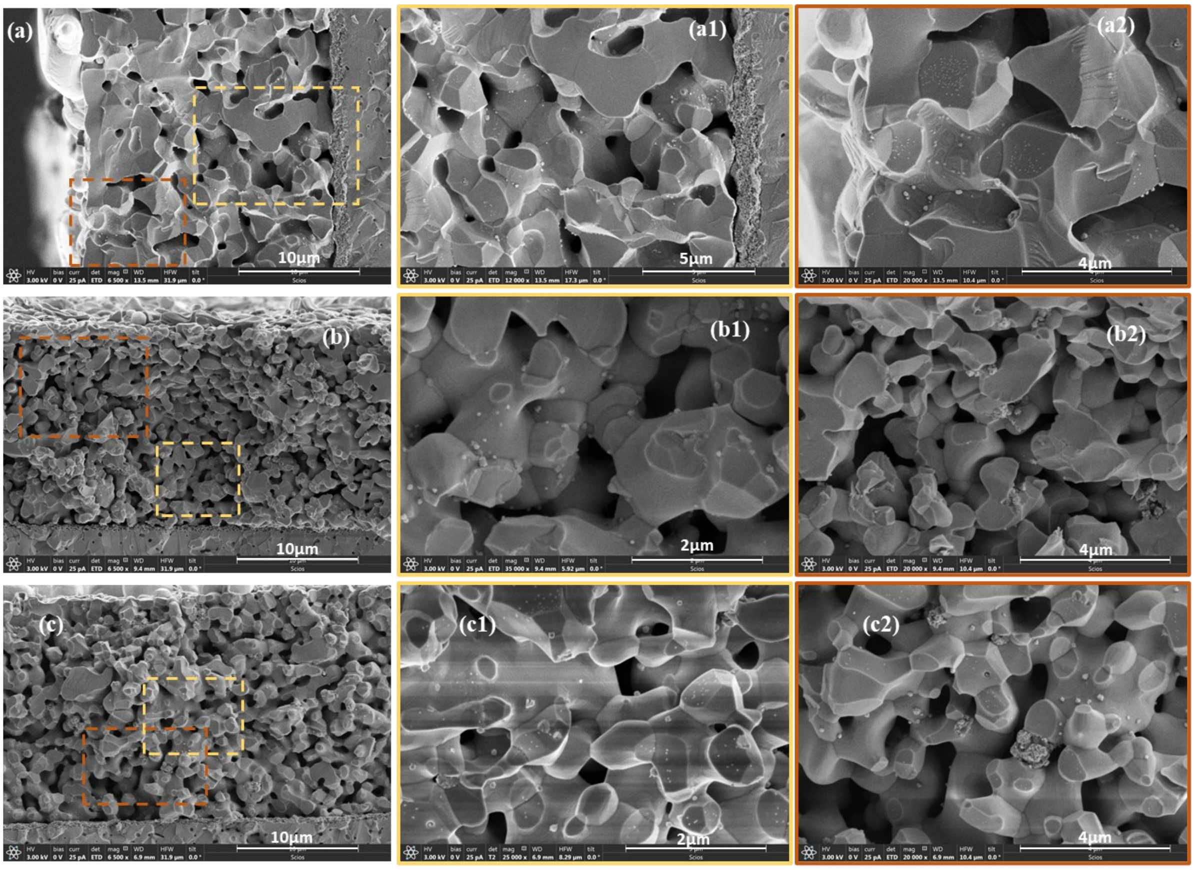

Figure 10. SEM micrographs of the cells with LCT-Ni6 (a, a1, a2), LCT-Ni3Co3 (b, b1, b2), and LCT-Ni5Co5 (c, c1, c2) fuel electrode after electrochemical testing. a1-2, b1-2, and c1-2 represent the close-up of framed areas in a, b, and c respectively

Noting in Figure 10 that the electrolyte develops some porous features (nanopores) at the vicinity of the fuel electrode/electrolyte interface, which is observed on all three cells after electrochemical testing. This phenomenon is related to the reduction of electrolyte under extremely high reducing conditions, such as above 2V in electrolysis operations (15, 16). In the present study, as it occurred at a minimum extent in all materials without observable difference and the fuel electrode seemed well attached to the electrolyte after electrochemical testing, it's not been taken into the scope of investigation.

Conclusions

In this work, we aimed to investigate the *operando* generation of nano-scaled electrocatalysts from the Ni and Co co-doped titanate perovskite as potential fuel electrode material in SOCs comparing to the only Ni doped titanate electrode materials. The Solely Ni doped titanate, $La_{0.43}Ca_{0.37}Ti_{0.94}Ni_{0.06}O_{3-\delta}$ (LCT-Ni6), and Ni-Co co-doped titanates, $La_{0.43}Ca_{0.37}Ti_{0.94}Ni_{0.03}Co_{0.03}O_{3-\delta}$ (LCT-Ni3Co3) and $La_{0.43}Ca_{0.37}Ti_{0.9}Ni_{0.05}Co_{0.05}O_{3-\delta}$ (LCT-Ni5Co5), were synthesized and characterized. These materials were adopted as fuel electrode in SOCs and subjected to electrochemical switching at 2V under electrolysis operation in pure CO_2 at 900°C, which was studied for *operando* activation of the materials' properties towards efficient CO_2 electrolysis and H_2 fuel cell.

It was found that all the compositions synthesized presented pure perovskite structure and the compositions having both Ni and Co showed larger unit cell parameters possibly due to incorporating the larger Co (II) ions into perovskite lattice. With Ni-Co co-doping, the titanates underwent higher mass loss during reduction in 5% H_2/N_2 comparing to the only Ni doped titanate. Additionally, the co-doped perovskite displayed higher conductivity than the solely Ni doped counterpart after reduction in 5% H_2/N_2 at 900°C. These indicated that the introduction of multivalent Co into the perovskite was beneficial in improving the extent of reduction of the titanate under the identical conditions. The electrochemical switching at 2V under CO_2 electrolysis operation was effective for generating nano-scaled electrocatalysts and enhancing the electrochemical activity of the fuel electrode. Nanoparticles from exsolution were observed on all the fuel electrodes after switching. However, due to the Co-doping changing the material's sintering behavior, optimizations are needed for tailoring the microstructure and/or the switching conditions for the Ni-Co co-doped titanate materials, to enable higher performance than the only Ni doped titanate.

Acknowledgments

The authors would like to thank the financial support from the EPSRC UKRI Innovation Fellowship EP/S001891/1 and the EPSRC Capital for Great Technologies Grant EP/L017008/1.

Supplementary data

Supplementary data is available Online or from the authors.

References

1. A. Hauch, R. Küngas, P. Blennow, A. B. Hansen, J. B. Hansen, B. V. Mathiesen, and M. B. Mogensen, *Science*, **370**, 6513 (2020).
2. J. T. S. Irvine, D. Neagu, M. C. Verbraeken, C. Chatzichristodoulou, C. Graves, and M. B. Mogensen, *Nat. Energy*, **1**, 15014 (2016).
3. P. A. Connor, X. Yue, C. D. Savaniu, R. Price, G. Triantafyllou, M. Cassidy, G. Kerherve, D. J. Payne, R. C. Maher, L. F. Cohen, R. I. Tomov, B. A. Glowacki, R. V. Kumar, and J. T. S. Irvine, *Adv. Energy Mater.*, **8**, 1800120 (2018).
4. S. P. Jiang, *Mater. Sci. Eng. A*, **418** (1–2), 199 (2006).
5. D. Neagu, G.Tsekoulas, D. N. Miller, H. Menard, and J. T. S. Irvine, *Nat Chem.*, **6**, 916 (2013).
6. D. Neagu, T. S. Ou, D. N. Miller, H. Menard, S. M. Bukhari, S. R. Gamble, R. J. Gorte, J. M. Vohs, and J. T. S. Irvine, *Nat. Comm.*, **6**, 8120 (2015).

7. D. Neagu, E. I. Papaioannou, W. K. W. Ramli, D. N. Miller, B. J. Murdoch, H. Ménard, A. Umar, A. J. Barlow, P. J. Cumpson, J. T.S. Irvine, and I. S. Metcalfe, Nat. Comm., **8**, 1855 (2017).
8. Y. Sun, Y. Q. Zhang, J. Chen, J. Li, Y. Zhu, Y. Zeng, B. S. Amirkhiz, J. Li, B. Hua, and J. Luo, *Nano Lett.*, **16**, 5303 (2016).
9. E. I. Papaioannou, D. Neagu, W. K. W. Ramli, J. T. S. Irvine, and I. S. Metcalfe, *Top. Catal.*, **62**, 1149 (2019).
10. T. Zhu, H. E. Troiani, L. V. Mogni, M. Han, and S. A. Barnett, *Joule*, **2**, 478 (2018).
11. Y. Sun, J. Li, L. Cui, B. Hua, S. Cui, J. Li, and J. Luo, *Nanoscale*, **7** (25),11173 (2015).
12. S. Liu, Q. Liu, and J. Luo, *J. Mater. Chem. A*, **4**, 17521 (2016).
13. J. Myung, D. Neagu, D. N. Miller, and J. T. S. Irvine, *Nature*, **537**, 528 (2016).
14. M. Chanthanumataporn, J. Hui, X. Yue, K. Kakinuma, J. T. S. Irvine, K. Hanamura, *Electrochim. Acta*, **306**, 159 (2019).
15. J. Schefold, A. Brisse, and M. Zahid, *J. Electrochem. Soc.*, **156**, B897 (2009).
16. M. Chen, Y. Liu, J. J. Bentzen, W. Zhang, X. Sun, A. Hauch, Y. Tao, J. R. Bowen, and P. V. Hendriksen, *J. Electrochem. Soc.*, **160**, F883 (2013).